IEEE Access
Multidisciplinary | Rapid Review | Open Access Journal

Received 16 April 2023, accepted 28 April 2023, date of publication 5 May 2023, date of current version 11 May 2023.

Digital Object Identifier 10.1109/ACCESS.2023.3273327

METHODS

3D Visualization of Pulmonary Vessel Based on Low-Cost Segmentation and Fast Reconstruction

QIANGHAO HUANG[1,2], LIN ZHANG[1], LILU LIU[1], YUQI CAO[1], HONGHAI MA[3], LUMING WANG[3], AND CHUNLIN ZHOU[1,4]

[1]College of Control Science and Engineering, Zhejiang University, Hangzhou 310027, China
[2]Huzhou Institute of Zhejiang University, Huzhou 313000, China
[3]The First Affiliated Hospital, Zhejiang University School of Medicine, Hangzhou 310003, China
[4]Binjiang Institute of Zhejiang University, Hangzhou 310014, China

Corresponding author: Chunlin Zhou (c_zhou@zju.edu.cn)

This work was supported by the Key Research and Development Program of Zhejiang Province, China, under Grant 2022C04030.

ABSTRACT Real-time visual-aided navigation and path strategy for pneumonoconiosis and efficient 3D visualization of pulmonary vessels are of great research and clinical significance in the treatment of lung diseases. The complex structure of lung tissue limits the application of deep learning in pulmonary vascular visualization due to the lack of vascular labeling datasets. Also, the existing methods have large computational complexity and are low efficiency. This study proposes a method for high-quality 3D visualization of pulmonary vessels based on low-cost segmentation and fast reconstruction, consisting of three steps: 1) Pulmonary vessel feature extraction from lung CT images using self-supervised learning, 2) Segmentation of pulmonary sparse vessels in lung CT images using self-supervised transfer learning, and 3) 3D reconstruction of pulmonary vessels based on segmentation results of step (2) using interpolation. The accuracy of pulmonary vascular contour segmentation was improved from 91.31% using the sparse coding to 98.65% using our proposed method (27,270 test sample points); the classifier evaluation accuracy was improved from 95.33% to 98.26%, and the average running time of the model with the test set data was 44 ms per slice. the segmentation results can automatically generate a complete vascular tree model with an average time of 10.8s $\pm$ 1 1.6s. The results demonstrate that the proposed method provides fast and accurate 3D visualization of pulmonary vessels, and is promising for more precise and reliable information for pneumonoconiosis patients.

INDEX TERMS CT image, pulmonary vessel, reconstruction, segmentation, 3D visualization.

I. INTRODUCTION

T lungs play a major role in the human respiratory and cardiovessel systems, and an important role in immune protection and endocrine metabolism. Lung cancer has the highest incidence and mortality of all cancers, 11.6% and 18.4%, respectively [1]. Research and development for lung cancer treatment methods are extremely important. With the rapid development of medical imaging, information technology, and machinery, pneumonoconiosis, characterized by small wounds and little pain and bleeding, has become one of the main treatments for lung diseases [2]. A doctor or robot penetrates the epidermis and targets the tumor according to the preoperative planning path. However, the physiological structure of the lung is particularly complex; it contains many blood vessels, air-filled alveoli, and other tissues, and is continuously retracting and expanding. Thus, pneumonoconiosis requires greater visual-aided navigation and path strategies. Especially during surgery, the main blood vessels must be avoided by the puncture needle to prevent serious pulmonary bleeding and other complications [3]. The large scale of multisource medical image data for the lung, difficulty in extracting specific targets, and non-intuitive imaging results produce preoperative difficulties and risks such as puncture needle path planning. A fast and accurate 3D visualization method for pulmonary vessels is required for image

The associate editor coordinating the review of this manuscript and approving it for publication was Vishal Srivastava.

assistance in puncture surgery to quantitatively reflect the correlation between tissue image features and the corresponding disease diagnosis, reduce the risk of internal bleeding, and improve the surgical success rate. The main components of 3D visualization are segmentation and 3D reconstruction of pulmonary vessels.

The difficulty of pulmonary vessel segmentation lies in the complex and diverse structure, the multiscale, high-noise, fuzzy boundaries, and low contrast with surrounding tissues. Mainstream vessel segmentation schemes can be divided into rule-based and machine-learning-based methods [4]. Rule-based methods utilize the photometric and structural characteristics of tubular structures. They rely on prior anatomical knowledge and require user participation during the operation. In machine-learning-based methods, transform segmentation tasks into pixel-classification problems. The feature of each pixel is considered to related to its neighborhood in traditional machine-learning methods. With the limited size of image blocks and the high overlap between them, traditional machine-learning methods lead to global feature loss and many redundant calculations, limiting segmentation performance. In contrast, deep-learning methods can automatically extract image features through a large number of training samples and efficient convolution combinations to predict the category of each pixel in the image in an end-to-end manner [5], [6]. However, with a lack of labeled datasets for training, application of deep-learning methods in pulmonary vessel segmentation has progressed slowly. Transfer learning provides an option for solving these problems [7], [8], [9]. A self-supervised transfer-learning method that can effectively overcome the lack of labeled data is proposed in this study, conducting model pre-training using a large-scale unlabeled lung CT image dataset and transferring the learned features to the sparse vessel segmentation task.

The 3D reconstruction of lung tissue can be divided into two types according to the processed data unit, pixels or voxels. Pixel-based 3D reconstruction methods are mainly used for 2D image sequences, such as x-ray sequences, in multiviews. Depth information is obtained through image correction, feature matching, cost aggregation and other operations to complete 3D reconstruction. Technical difficulties arise as the internal and external parameters of the acquisition device are unknown and the geometric information of the scene is unknown. The key step is obtaining the required geometric information through feature extraction and matching by searching for image pairs with overlapping scenes in 2D image sequences obtained from different views. Methods such as orthogonal polynomials (OPs) [10], [11], Krawtchouk moments [12], discrete tchebichef polynomials [13], [14] and Hahn polynomials [15], [16], [17] can extract image features. According to the obtained geometric information and environmental parameters, the disparity (target depth) is obtained for the 3D reconstruction [18], [19]. The 2D image sequences have hardware requirements for medical image acquisition, such as C-arm and U-arm x-ray machines. Regular x-ray machines cannot obtain clear vessel images; machines that meet the imaging needs are not widely available. 3D reconstruction methods that process voxels are aimed at obtaining volume element sets, such as CT image sequences, by downsampling the 3D space, and can be divided into volume- and surface-rendering methods. Volume-rendering reconstructs the entire 3D model including its internal structure. Although volume-rendering is relatively slow, the results contain comprehensive information that is helpful for doctors in diagnosis. In comparison, surface-rendering only reconstructs the surface of the target model, which is relatively fast but does not provide 3D information for the internal structure [20], [21]. The medical problems addressed in this study do not require imaging of the internal vessel structure, but do require fast reconstruction speed; thus, we chose surface-rendering. Surface-rendering methods generate mesh patches based on spatial point-cloud data. To optimize details such as fusion, splicing, and texture mapping, scattered point sets must be searched and reconstructed. The complexity of this method is high; several minutes to tens of minutes are generally required to process the data, not suitable for providing quickly reconstructed intraoperative images for assistance in pneumonoconiosis [22], [23], [24]. To meet the requirements for reconstruction efficiency in pneumonoconiosis, segmentation-based surface 3D reconstruction is proposed for rapid 3D reconstruction of pulmonary vessels. It interpolates the ordered sequence of the segmented vessel contour to make the point-cloud denser, reducing the time for reconstruction of unordered point sets.

In summary, an efficient visualization method for pulmonary vessels is proposed to avoid surgical failure caused by accidental contact of the puncture needle with vessels during pneumonoconiosis. First, a lung vessel segmentation method based on self-supervised transfer learning is proposed. This method does not require a large number of labeled samples. A small number of discrete labeled points are used as supervision information, and a strategy of feature extraction and classification training in stages is proposed. The self-supervised pre-training model was used as the feature extractor to determine the best model combination for completing fine segmentation of pulmonary vessels. Second, a segmentation-based pulmonary vessel reconstruction method is proposed. This method does not require a large number of reconstruction calculations for disordered point sets. Based on the segmentation results of the pulmonary vessels, the ordered point-clouds were densified using different interpolation strategies to complete surface reconstruction. The vessel segmentation and 3D reconstruction time were shortened.

The contributions and innovations of this study include:

1. We designed the pre-training model as an image restoration task which can reduce the cost of labeling. The original image is transformed and input into the model. The training model restores the original image through two stages: feature extraction and image reconstruction.We selected five types of

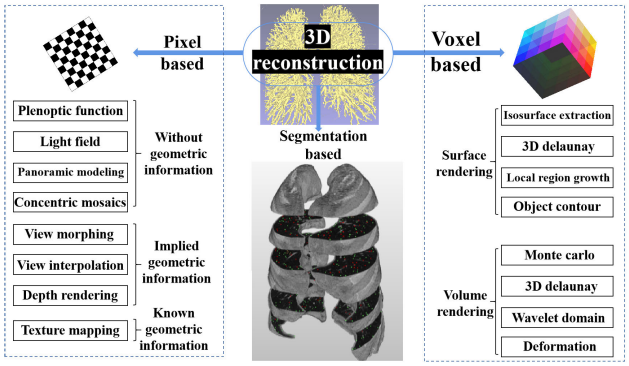

FIGURE 1. Summary of the related works.

transformations, such as nonlinear transformation and local pixel reorganization, to make the model have better feature extraction performance.

2. We proposed a pulmonary vessel segmentation framework based on self-supervised transfer learning. The vessel pixel classification model was trained based on pre-training model and image label information. The problem of dense vessel segmentation is transformed into discrete vessel point classification, which further reduces the labeling cost.

3. We proposed a fast 3D vascular reconstruction method based interpolation, which mainly considers the shape, size, and change ratio of inter-layer contours of vessel. After interpolating to obtain sufficient inter-layer vessel contours, we sequentially connect these contours, and the pixels on these contours are dense 3D point sets that can be used to complete surface reconstruction.

The remainder of this paper is organized as follows. In Section II, current pulmonary vessel segmentation and 3D reconstruction methods are reviewed. The method proposed in this study is described in detail in Section III. Section IV presents the experimental results using the methods proposed in this study on public and private datasets. A summary is provided in Section V.

II. RELATED WORKS

A. PULMONARY VESSEL SEGMENTATION

In recent years, various automatic segmentation algorithms for pulmonary vessels have been proposed [24]. Using Hessian matrix eigenvalues, Sato and Frangi et al. [25], [26] constructed discriminant functions and successfully distinguished tubular, planar, and spherical structures in images for the first time, and they proposed take vascular enhancement as a filtering process to find tubular geometric structures. In VESSEL12 vascular segmentation challenge, most methods based on Hessian matrix enhancement also showed good performance [27]. However, Hessian matrix methods have poor enhancement effects on irregular tubular vessels. The intensity-based method distinguishes vascular and non-vascular elements directly according to pixel values, mainly including threshold method and region growing method. Lassen et al. [28] converted the original CT image into a binary image using a single threshold in their work. Voxels higher than the threshold are considered as blood vessels, otherwise as non-vascular vessels. Due to the large difference in gray values of pulmonary vessels, the accuracy of this method is low. The region growing algorithm was proposed by Adams and Bischof [29]. In this algorithm, similar pixels are combined into regions based on their attributes, such as intensity. The segmentation result of this method depends entirely on the setting of seed points and growth rules. Due to image noise and local volume effect, the intensity-based segmentation often gives false recognition [30]. For this reason, Kaftan et al. [31], proposed the concept of fuzzy segmentation which combines threshold information and fuzzy connectivity method to segment pulmonary vessels. The eigenvalue of Hessian matrix was used to constrain the region growth [32]. Other approaches include graph cut method and other graph-based model based vessel segmentation methods, which rely on prior knowledge and parameter adjustment. Such methods cannot extract small blood vessels with low contrast, involve a lot of iterative calculations, and suffer from slow segmentation speed [32], [33], [34], [35]. Among traditional machine learning methods, Zhao et al. [36] extracted features by designing a sparse automatic encoder and then used a random forest classifier to segment pulmonary vessels. Hessian features and Adaboost classifier were used to segment pulmonary vessels [37].

The method based on deep learning can automatically learn without manually designing feature extraction methods. Various convolutional neural network framework were uesd to extract pulmonary vessels and combined it with the region growth method to solve the problems of discontinuity and false positive in vessel segmentation results. Such as the cascaded [38], the stacked [39]. Wang et al. [40] combined convolutional neural network, principal component analysis, probability tracking framework and other methods to extract the entire vascular tree.

B. PULMONARY VESSEL 3D RECONSTRUCTION

The information needed for 3D vascular reconstruction mainly comes from volume data represented by medical images such as CT. Voxel-based 3d reconstruction methods can be divided into surface rendering and volume rendering. Surface rendering mainly includes surface reconstruction algorithm based on isosurface extraction, triangular patches, local growth and contour lines and so on. For surface reconstruction based on distance field isosurface extraction, representative algorithms include Poisson surface reconstruction algorithm [41], Hoppe's surface reconstruction algorithm based on unordered points [42], Chen Shen's surface estimation algorithm based on unordered polygon elements [43], etc. Based on the 3D Deloitte triangulation reconstruction algorithm, the representative algorithms include the weight shell of Ament and the 3D of Edelsrunner α Model algorithm [44], etc. Reconstruction algorithms based on local region growth algorithm. include Bernardini's

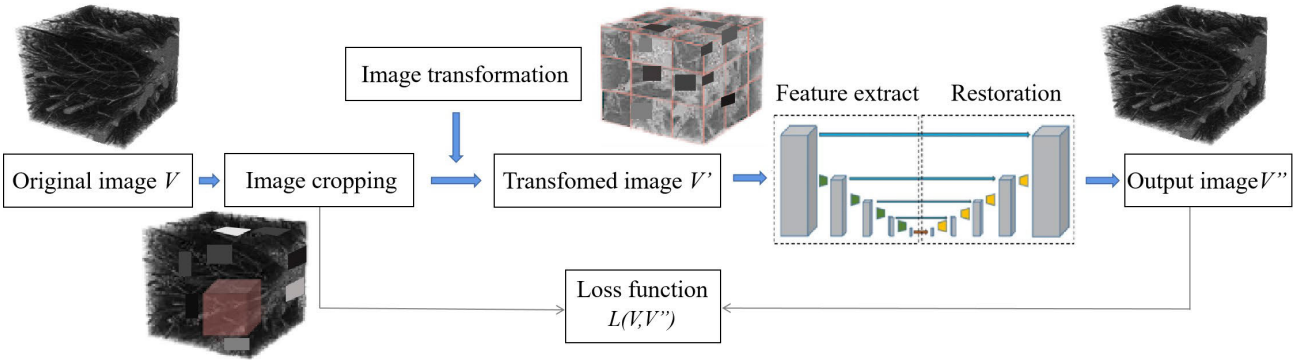

FIGURE 2. Self-supervised feature extraction model framework.

rolling ball algorithm [45] and Kuo's region growth algorithm based on deloitte triangulation [46]. Based on target contour reconstruction algorithms, typical algorithms include Keppel's complex surface estimation based on contour triangulation [47] Kedem's optimal surface estimation based on contour [48] and virtual shell technology. In volume rendering, there are Monte Carlo volume rendering algorithm, fractal volume rendering algorithm, volume rendering algorithm based on wavelet domain, etc. If the image space is taken as the order, the most typical method is ray casting [49]. When the order is object space, the most typical methods are snowball throwing [50], stagger cutting deformation, etc.

3D reconstruction of clinical medical images has been widely used in various parts of the human organs and blood vessels. Guggenberger et al. [51] located vessels in Magnetic Resolution Imaging (MRI) images, and directly reconstructed intracranial vessel trees using regional growth method with existing software; Centerline prediction method was used to extract intracranial vessels for MRI images [52]; Kigka et al. [53] conducted semi-automatic vessel visualization for computed tomography angiography (CTA) images of coronary arteries; region growth and marching cube method was used to reconstruct carotid artery CTA images [54]; the end-to-end 3D convolution network was used to realize the vessel reconstruction based on the intracranial CTA image [55], and shortened the time to 4.94 $\pm$ 1 0.36 minutes; The model proposed by Li [56] and others focuses on extracting lung information from complete human body information. In terms of reconstruction, the research on lung tissue reconstruction is less than that of other organs, and even less is the method with outstanding performance in reconstruction speed, accuracy and automaticity. Among them, timeliness is still the primary focus of intraoperative imaging guidance and academic research.

In general, compared with traditional algorithms in image processing, methods based on machine, especially deep neural networks, can significantly improve the accuracy and robustness of pulmonary vessel segmentation, though they usually require a large number of training data. In the field of medical images, can be reduced by combining the application of self-supervised learning and transfer learning. In this paper, we propose an efficient method for visualizing pulmonary vessels that aims at quick and accurate segmentation and reconstruction of pulmonary vessels from more commonly used images in pulmonary disease treatment, i.e. CT image sequence, not needing angiography.

III. PROPOSED METHOD

The method for 3D visualization of pulmonary vessels proposed in this paper includes three steps: feature extraction of the pulmonary vessels based on self-supervised learning; sparse vessel segmentation based on transfer learning; 3D reconstruction of the vessels based on segmentation. Details of each step are described below.

A. FEATURE EXTRACTION OF THE PULMONARY VESSELS BASED ON SELF-SUPERVISED LEARNING

The extraction of pulmonary vessel features using the self-supervised learning model was designed as an image restoration task. As shown in Fig. 2, the original image was fed to the model after cropping and transformation. The training model was able to recover the original image through feature extraction and image reconstruction. The self-supervised learning pre-training model in this paper has 53 layers, including 27 layers for the upsampling path and 26 layers for the downsampling path. The end of the model is composed of a $1 \times 1 \times 1$ convolution layer and a sigmoid activation function. The stride of the above operation on the three dimensions of the image is set to 2. In this way, the original 512×1512 image itself became label to supervise the model training. To complete this task, the model needs to learn to recognize universal low-level visual features and high-level semantic features from the image, so that the model can be generalized to a variety of downstream tasks.

3D U-Net [57] was selected as the backbone network for self-supervised learning since the downsampling and the upsampling parts of it comprehensively contain the feature extraction and image reconstruction functions, respectively. It differs from the standard U- Net in that batch normalization (BN) is introduced before each ReLU, which is used to normalize the mean and the standard deviation of each batch in the training process to accelerate the convergence

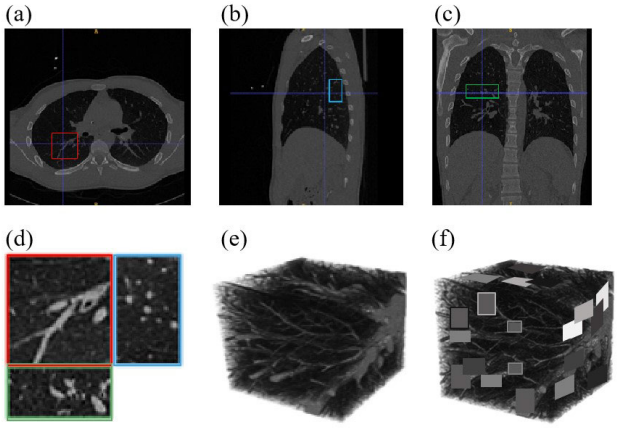

FIGURE 3. Original Data Cropping. panels (a), (b), and (c) show the cropping windows corresponding to the transverse, sagittal, and coronal planes of the same local vascular region. Panel (d) shows the combined views of the three cropping windows, panel (e) shows the original volume data in 3D space, and (d) shows the schematic diagrams of cropping windows in 3D space.

of the model. In addition, 3D U-Net introduces a weighted softmax loss function. The weight of the background in the loss expression is decreased and the weight of the target is increased so that the model can obtain a good feature representation from sparse annotation data, which is then extended to the entire 3D image. By setting the weight of the unlabeled pixels to zero, learning can be restricted to occur only from the marked pixels. Image cropping in the framework of the self-supervised feature extraction model is shown in Fig. 3.

In the downsampling path, each layer contains two convolution operations of $3 \times 3 \times 3$. After each convolution, a linear correction unit (ReLU) is added. After every two convolutions, a maximum pooling of $2 \times 2 \times 2$ is performed. In the upsampling path, each layer first performs a $2 \times 2 \times 2$ deconvolution operation then performs two 3×3 convolutions and corresponding ReLU operations. In the last layer, a convolution operation of $1 \times 1 \times 1$ reduces the number of output to the number of labels, and finally obtains the probability segmentation image of the same size as the original image. In the downsampling path, the lung image block is extracted from low-level to high-level features, such as color, edge to region, and category, through a layer-by-layer convolution network. In the upsampling process, the pixel position and resolution of the output image are gradually reconstructed according to the training task. At the same time, the characteristic image of the encoder part is directly transferred to the decoder part through cross-level connection, which improves the model accuracy and solves the problem of gradient disappearance.

Considering the characteristics of the lung CT images after cropping, five image transformation methods [58], nonlinear transformation, pixel shuffle, random window, inpainting, and denoising were selected to transform the cropped images while comprehensively taking into account the image intensity, shape and appearance, local texture, spatial context, and other aspects to generate pseudo tags.

Let us assume the input set of the model to be $\chi = \{x_1, x_2, \cdots, x_n\}$, which includes n CT image blocks.On applying the transformation function $f(\cdot)$ to these image blocks to generate:

$$\tilde{\chi} = f(\chi) \tag{1}$$

where $\tilde{\chi} = \{\tilde{x}_1, \tilde{x}_2, \cdots, \tilde{x}_n\}$ denotes image blocks after transformation. Taking $\tilde{\chi}$ as the input to the learning function $g(\cdot)$ through the 3D U-Net network with encoder decoder structure to map the transformed image block $\tilde{\chi}$ back to the original χ:

$$g(\tilde{\chi}) = \chi = f^{-1}(\tilde{\chi}) \tag{2}$$

The five image transformation methods were used independently and combined randomly to facilitate the model to learn more comprehensive feature representation. The results obtained after these transformations are shown in Fig. 4.

B. PULMONARY VESSEL SEGMENTATION BASED ON SELF-SUPERVISED TRANSFER LEARNING

In this study, we proposed a strategy for feature extraction and classifier training in stages, and designed a framework for the pulmonary vessel segmentation algorithm based on self-supervised transfer learning. As shown in Fig. 5, the self-supervised pre-training model of module I was transferred to module II as a feature extractor to obtain the feature vector of each vessel or non-vessel label point. In module II, these feature vectors and labels of the labeled points were used as the input data, and the classifier was trained to correctly recognize pulmonary vessel pixels corresponding to pulmonary vessels.

Logistic Regression(LR) was selected as the classifier for the baseline model. The labeled point labels and corresponding feature vectors were used as the input for the LR classifier. After the classifier training, pulmonary vascular prediction could be performed on the entire image. For the binary classification task, the data was given as $D = (x_1, y_1), (x_2, y_2), \cdots, (x_N, y_N), x_i \subseteq R^n, y_i \in 0, 1, i = 1, 2, \cdots, N$ Assuming that there is a straight line that makes the data linearly separable, the decision boundary could be expressed as $z = XW = w_0 + w_1x_1 + w_2x_2 + \cdots + w_Nx_N$. LR was performed using the logarithmic probability function $g(z) = \frac{1}{1+e^{-z}}$, and the predictive value z of linear regression was mapped, so that the value space of the objective function is mapped from $(-\infty, +\infty)$ to (0,1). For a sample point, if $z = xW > 0$ after mapping and the value of the logarithmic probability function $h > 0.5$, it is considered to be 1, otherwise it is considered to be 0.

First connect the vessel points obtained from the model related to the minimum linear distance, and local binary fitting was performed on the contour of the closed area thus formed. It was necessary to integrate all the minimized single-pixel energy functions. In the corresponding experiments in this section, the experimental results were evaluated

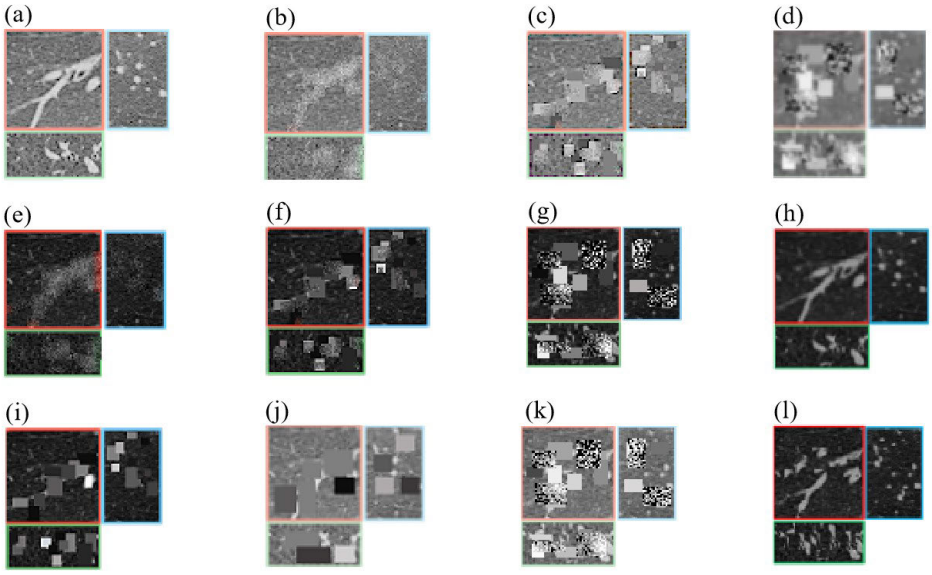

FIGURE 4. Output of image transformation. $f_N(\cdot)$ represents the image transformation function, a represents nonlinear transformation, b represents pixel shuffle, c represents random window, d represents image inpainting, and e represents image denoising(Gaussian noise was added to the image in this study). (a) represents using nonlinear transformation on image V, i.e.. $f_a(V)$. Similarly, (b) represents $f_{a,b}(V)$, (c) represents $f_{a,b,c}(V)$, (d) represents $f_{a,b,c,d,e}(V)$, (e) represents $f_b(V)$, (f) represents $f_{b,c}(V)$, (g) represents $f_{b,c,d}(V)$, (h) represents $f_e(V)$, (i) represents $f_c(V)$, (j) represents $f_{a,c}(V)$, (k) represents $f_{a,b,c,d}(V)$, (l) represents $f_d(V)$.

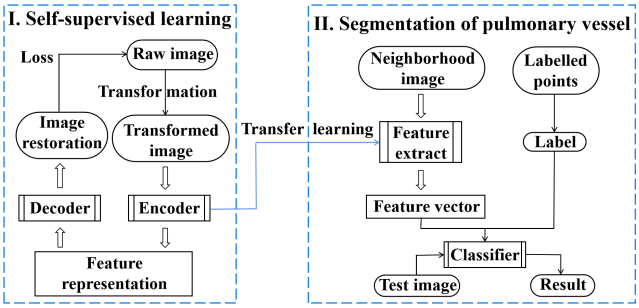

FIGURE 5. Pulmonary vessel segmentation framework based on self-supervised transfer learning.

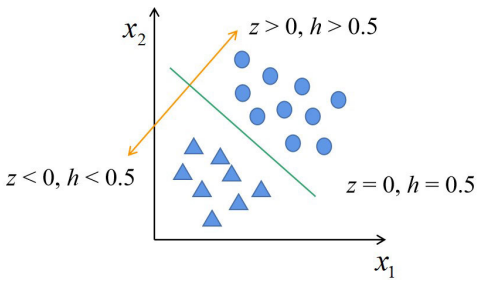

FIGURE 6. Schematic diagram of logistic regression.

using ACC and ROC indicators as given below.

$$Accuracy(ACC) = (TP + TN)/(TP + TN + FP + FN) \tag{3}$$

If the instance is positive (vascular point) and predicted to be positive, it is true positive (TP). If the instance is positive but predicted to be negative (non-vascular point), it is false negative (FN). If the instance is negative but predicted to be positive, it is false positive (FP). If the instance is negative and predicted to be negative, it is true negative (TN). The area under the curve (AUC) under the receiver operator characteristics(ROC) represents the performance of the classification model, reflecting the proportion of the model ranking the positive examples before the negative examples.

C. 3D RECONSTRUCTION OF THE PULMONARY VESSELS BASED ON SEGMENTATION

For the segmentation results of the vessel contours obtained in steps A and B, such as the local contour C in a layer of CT image, it was necessary to find the corresponding local contours C_1 and C_2 in the two adjacent CT images before interpolation reconstruction. In this paper, the multi-scale indices of curve shape error, closed contour area, and lateral distance from the center point were selected to match the local contours between adjacent CT images. for the pixel points on the CT image sequence defined as (x, y, z), let c be the contour curve $f(x)$ of a certain vessel on the $z - th$ CT image, and let the curve set on the adjacent $z - th + 1$ CT image be C. From a selection of any n points on curve c, any 3 of these n points can be form a triangle by connecting each of them. The center of gravity of each triangle can be calculated to obtain $P_1, P_2, \ldots, P_n$. Using the concept of K-nearest neighbors, the mean value of the three coordinate dimensions was calculated to obtain the approximate center

Algorithm 1 Patch Generation and Interpolation

Require:
Input1: VoxelData c_n
Input2: float isoLevel

Require:
Output1: P_{c_n}
Output2: $Cross - section_n$

while Patch bounding spans generated between every two slices exceed 270 degrees **do**
  for $c, c' inrange(c_n)$ **do**
    for $Pinrange(c)$ **do**
      for $P', P'' inrange(c')$ **do**
        $P_n append(generate(P, P', P''))$
      end for
    end for
  end for
  $Cross - section_n = Cross - section(P_n)$
  $P_{c_n} = centre - extract(Cross - section_n)$
end while

P_1 of the graph enclosed by curve C. Approximations to the center of all the other contours were calculated in a same manner. The lateral distance error $errC$ of the center point is defined as:

$$errC = \left|P_1 - P_n'\right| \tag{4}$$

The closed contour area S can be obtained by definite integration of the curve equation:

$$S = \int_a^b \left(C\left(x\right)_{max} - C\left(x\right)_{min}\right) dx \tag{5}$$

The area error $errS$ of the closed contour is defined as:

$$errS = \left|S_1 - S_n'\right| \tag{6}$$

The curve shape error $errL$ is defined as:

$$errL = \int_a^b MAX(|C(x)_{max} - C'(x)_{max}|, |C(x)_{min} - C'(x)_{min}|)dx \tag{7}$$

The vessel contours between adjacent CT images can be matched based on the minimum value of the contour curve-matching cost function. One set of m points, P_1, and another set of n points, P_2, were reandomly selected from the two matching contour curves c_1 and c_2, respectively. A triangular patch can be formed by taking 1 point from point set P_1 and 2 points from point set P_2, or 2 points from P_1 and 1 point from P_2. Fig. 7 shows a locally enlarged view of the interpolation patch along the direction of the cross-section.

The triangular patch mesh generated was actually the reconstructed surface between the contour curves of adjacent CT images. The precision of the reconstruction is directly related to the number of the generated triangles. Increasing the number of triangles gives a denser mesh and makes the restored details more accurate, while more reconstruction time is needed.

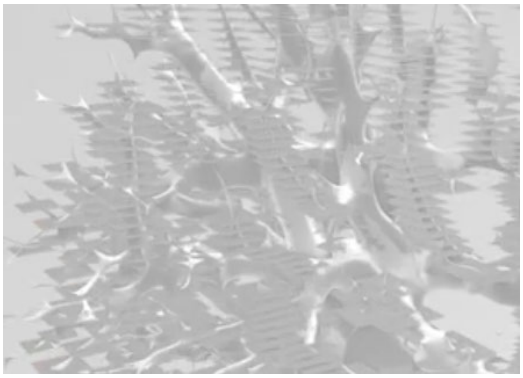

FIGURE 7. Interpolation patch in the cross-section direction.

At the same time, the contours of vessels were connected head to tail to obtain the interpolated contours between the adjacent CT images. The contours that were very close to each other were surfaces. Therefore, the generation of triangular patches for these was essentially the process of surface reconstruction. The triangular mesh thus generated needed further processing, including fusion, smooth denoising, splicing, texture mapping, etc.

IV. EXPERIMENTS AND RESULTS

This section describes the preparation of the experimental data and results of the three steps described in the previous section. This experiment was based on the large LUNA16 public dataset of lung CT images for self-supervised model pre-training. LUNA16 is a pulmonary nodule detection dataset released in 2016 with data derived from LIDC-IDRI, the largest currently available pulmonary nodule dataset. The LIDC-IDRI includes 1,018 cases from seven academic institutions. Consequently, there is significant diversity in the scanning instruments used and their related parameters. Each case consisted of chest CT scan images and corresponding XML tag files. The LUNA16 dataset excludes low-definition CT scans with slice thicknesses greater than 2.5 mm, and CT scans with inconsistent slice spacing or missing sections, including 888 low-dose lung CT scans. Each CT scan is a three-dimensional image in the.mhd format, with different numbers of slices that vary with different scanning instruments, scanning slice thickness, and patients.

A. FEATURE EXTRACTION OF PULMONARY VESSELS

First, 700 CT sequences were selected from the LUNA16 dataset, and 20 64 × 64 × 32 image blocks at different positions were randomly cropped in each CT sequence as an unlabeled image training set. To learn image features more specifically in the training process, it was necessary to preprocess the image blocks, which included clipping the intensity of all CT images to be within the range of [−1000, 1000]

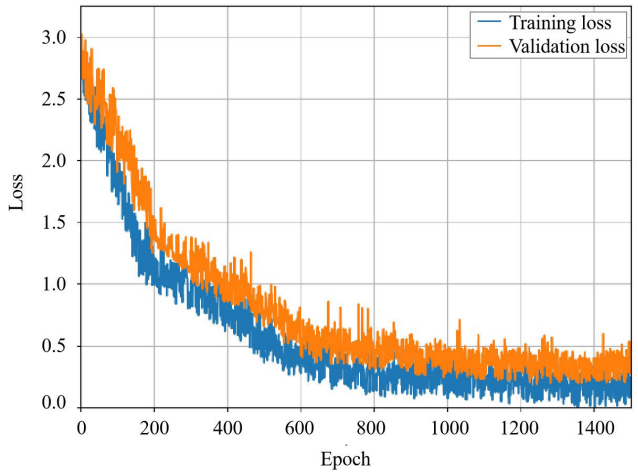

FIGURE 8. Learning curve of model training.

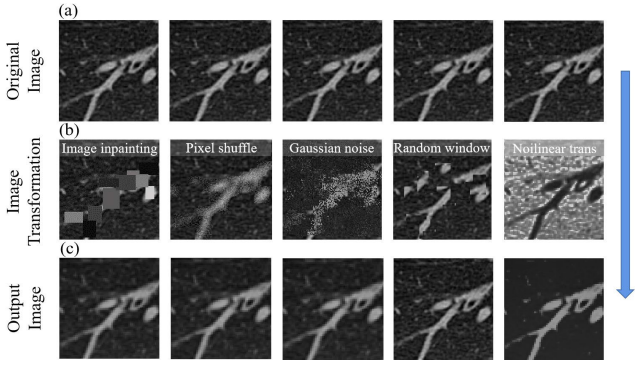

FIGURE 9. Comparison of the input and output images. (a) represents the original image, (b) represents five image transformation effects, (c) represents the output image of the self-supervised feature extract model.

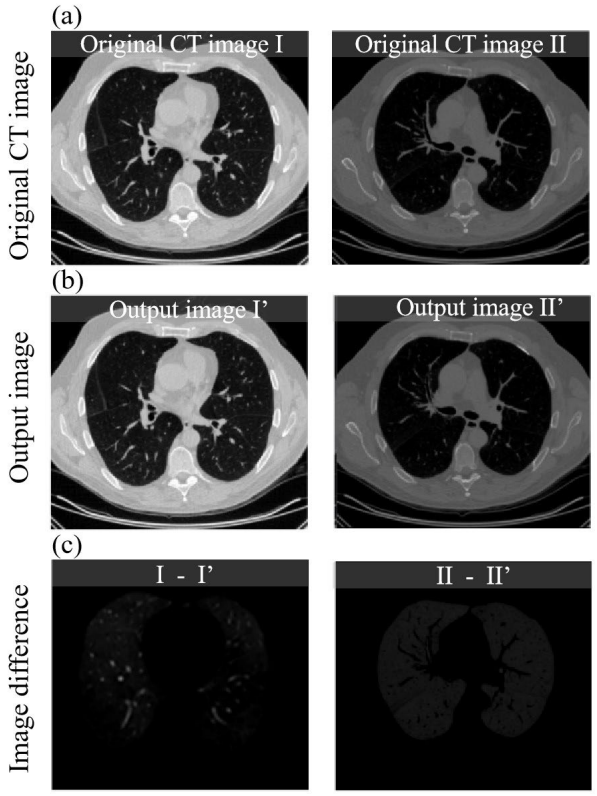

FIGURE 10. Comparison of output and input of self-supervised feature extraction model. (a) represents tow different original CT image, (b) represents their output respective, (c) represents the difference between the original and output image.

HU, normalizing them on a scale of [0, 1], and removing any image blocks that were either all 0 or all 1 after normalization. This provided 12,600 3D image blocks suitable for use as the training set. Following these steps, 3,400 3D image blocks were selected from 188 CT scans as the test set.

The Python package Keras was used for model training, and Adam was used as the optimizer, set to 0.93 and 0.99, respectively. The initial learning rate was set to 0.0001, and the batch size was set to 64. To prevent overfitting, an early stopping mechanism was proposed. If the loss value did not decrease for 40 consecutive epochs, model training was automatically stopped.

The training curve of the self-supervised learning model for the LUNA16 dataset is shown in Fig. 8. The errors in the training set and verification sets both decreased steadily; after approximately 1,500 iterations, they converged to 0.25 and 0.5, respectively. Clearly, this model is effective for training. Absence of overfitting reflects the strong learning ability of the self-supervised learning model.

As shown in Fig. 9, the output image of the model after the five image transformations is similar to the original image; the difference between them is small. This shows that the model has good image reconstruction ability, indirectly reflecting that the model has comprehensive and universal feature representation and can provide a strong feature extraction capability for downstream tasks.

As shown in Fig. 10, by subtracting the reconstructed output image from the learning model from the original CT image, it is observed that the image output from the model is similar to the original image; the difference between them is small. This shows that the model has good image restoration capability, indirectly reflecting that the model has comprehensive and universal feature representation and can provide a strong feature extraction capability for downstream tasks.

B. PULMONARY VESSEL SEGMENTATION

The pulmonary blood vessel segmentation dataset used in this experiment consisted of labeled data provided by VESSEL12 and hospital experts. VESSEL12 provides 23 CT sequences from diverse sources with different scanning parameters and is stored in the meta (.mhd/raw) format. Each CT had 400 to 500 sections, with a section spacing of 0.59 mm and 0.89 mm and a resolution of 512 × 512. In this study, we used the capital letter V and CT serial number to distinguish between the 23 CT sequences. While none of the CT sequences from V1 to V20 provided annotation data, CT sequences

TABLE 1. Summary of pulmonary vascular labeling data.

CT Dateset	anno layers/slices	TP	NP	Total
V21	3/459	78	199	277
V22	3/448	98	192	290
V23	3/418	105	210	315
S1	400/448	13454	13816	27270
S2	110/188	2595	2660	5255
S3	120/189	3046	3112	6158

TABLE 2. Input 16 × 16 × 16 training images, and output the corresponding accuracy of each encoder layer for vascular pixel classification.

OUT Layers	Dimension	ACC	AUC
1	32×16×16×16	0.9435	0.9207
2	64×16×16×16	0.9444	0.9216
3	64×8×8×8	0.9491	0.9290
4	128×8×8×8	0.9605	0.9457
5	128×4×4×4	0.9152	0.8912
6	256×4×4×4	0.9096	0.8829
7	256×2×2×2	0.8814	0.8574
8	512×2×2×2	0.8644	0.8284

labeled V21-23 provided .csv files containing 277, 290, and 315 annotation points, respectively, to illustrate the annotation process. The storage format of the labeled points was (x, y, z, label), where (x, y, z) is the three-dimensional coordinate of the labeled points. The label for the points of the blood vessels was 1, and the label for non-blood was 0.

V21, V22, and V23 in Table 1 represent CT scans with serial numbers 21, 22, and 23, respectively, in the VESSEL12 dataset. S1 represents V22 with expanded annotation data; S2 and S3 are CT sequences obtained from the hospital site.

In total, 592 labeled data points from V21 and V23 were used for model training; the remaining data in Table 1 were used as the test dataset. During the test, each label point of S1, S2, and S3 was checked to see if it was correctly assigned a label of 1 or 0 corresponding to vessel and non-vessel regions, respectively, in the segmentation result. As areas containing blood vessels can be ambiguous in thick-slice CT scans, accurate blood vessel segmentation requires thin-slice data. The CT scan slice thickness for V21-23 was 0.7 mm, which is suitable for blood vessel segmentation tasks. However, S2 and S3 were limited by suboptimal hospital equipment settings with a slice thickness of 2 mm, which challenged the generalization of the model.

When the output feature dimension is fixed, the classification accuracy of the model increases with a decrease in the size of the input image. With an increase in the number of layers, the accuracy of classification first increased and then gradually decreased from the fourth layer onward. This is because pulmonary vessel segmentation is based on local basic features such as edge and intensity. Thus, use of shallow features to classify vessel pixels can yield superior results. By entering a 16 × 16 × 16 training image, the output characteristics of eight encoder convolution layers from Conv0 to Conv7 were extracted to train and evaluate the LR model.

TABLE 3. Classification performance corresponding to different dimensions of feature vector.

OUT Layers	Dimension reduction	ACC	AUC
1	32×4×4×4	0.9597	0.9471
2	64×4×4×4	0.9687	0.9533
2	64×2×2×2	0.9742	0.9606
3	64×4×4×4	0.9774	0.9667
3	64×2×2×2	0.9831	0.9750
4	128×4×4×4	0.9887	0.9833
4	128×2×2×2	0.9843	0.9817

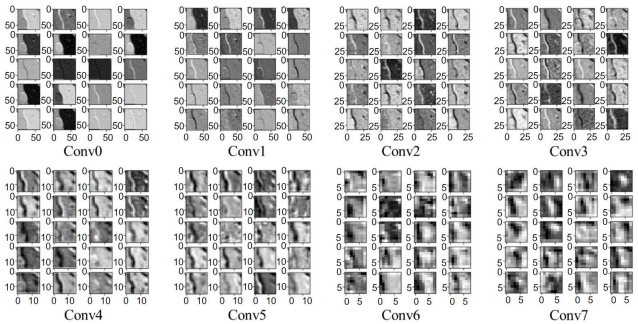

FIGURE 11. Feature extraction visualization of each layer of encoder.

TABLE 4. Performance comparison of different classifiers.

Model	ACC	AUC	Time
LR	0.983	0.963	44ms
SVM	0.948	0.937	102ms
RF	0.962	0.944	132ms
DNN	0.953	0.939	163ms

The feature vector outputs from the first six layers of the encoder were clipped, and feature vectors from the 4 × 4 × 4 neighborhood and 2 × 2 × 2 neighborhood of the central pixel were extracted under each channel. The classifier was retrained and its accuracy was evaluated. The experimental results are presented in Table 3. The 128 × 4 × 4 × 4 feature vector obtained by trimming the output features of encoder Conv4 achieved the best classification on the V22 test data, with ACC and AUC indicators of 0.9887 and 0.9833, respectively.

Feature extraction visualization is shown in Fig. 11.

After obtaining reliable vessel features, segmentation and classifier experiments were conducted. For all labeled data in the training set, 16 points considered as the center × 16 × 16 neighborhood image blocks were input into the self-supervised pre-training model; the output of the fourth convolution layer was used as the feature vector for the central annotation point. The LR, Support Vector Machine (SVM), Random Forest (RF), and Deep Neural Network (DNN) were used as classifiers; the labels and feature vectors of the annotation points were used for supervised learning. Subsequently, 27,270 labeled vessel point/non-vessel point data on the S1 test CT were classified and assessed. The results are presented in Table 4; the time indicator represents the average time required by the corresponding model to classify the test set.

TABLE 5. Classification accuracy of marked points in test dataSet.

CT Dataset	Label points	ACC	AUC
V22	290	0.9887	0.9833
S1	27270	0.9865	0.9826
S2	5255	0.9767	0.9738
S3	6158	0.9786	0.9754

TABLE 6. Classification accuracy of sparse coding.

CT Dataset	Label points	ACC	AUC
V22	290	0.9238	0.9720
S1	27270	0.9131	0.9512
S2	5255	0.8132	0.8377
S3	6158	0.8086	0.8295

From the perspective of prediction accuracy, although the ACC and AUC of LR are slightly higher than those of the other three classification algorithms, the difference in classification accuracy between the four algorithms is very small, indicating that the feature extractor is effective in extracting the discriminant features of pulmonary vessels sufficient for accurate classification.

For the labeled point data of the test set, the neighborhood $16 \times 16 \times 16$ image was input into the feature extractor, and the feature vector was input into the trained LR classifier to obtain the classification results of the labeled points. Real tags were used for evaluation. For complete vessel tree segmentation, it was necessary to cut the original CT image into an image block of size $16 \times 16 \times 16$ according to the sliding window, and input the feature extractor. The feature vectors of all non-edge voxel points were obtained simultaneously, and the LR model was used to predict the probability that each voxel point was a blood vessel. The complete vessel-tree segmentation result was obtained by setting a probability threshold.

The segmentation results for the vessel pixel points obtained by the classifier are presented in Table 5. For S1 labeled data, the classification effect was similar to that of V22, which shows that although V22 labeled data are few, they represent the vessel features of the CT image well. For S2 and S3, although the classification accuracy was lower than that of V22 and S1, considering that the former was from actual hospital data and that the 2-mm slice thickness significantly increased the difficulty of blood vessel segmentation, we believe that the classification can achieve the expected efficacy and accuracy, and that the model has some level of generalization ability.

Konopczynski [59] extracted features through 3D sparse coding and used a logistic regression classifier to detect vascular and nonvascular voxels, obtaining the highest score in the VESSEL12 Challenge. From the experimental results, the sparse coding algorithm achieved good results in pulmonary vascular segmentation on S1, but the effect was poor for S2 and S3. The self-supervised transfer-learning method in this study was based on pre-training of large lung CT images; the acquired features were more comprehensive and extensive.

FIGURE 12. Visualization results of vessel segmentation. The red circle in (a) represents the recognition of vascular points, the blue circle represents the recognition of non-vascular points, (b) represents the segmentation results of the vessels in 2mm thick CT images, and (c) represents the segmentation results of vessels in 0.7mm thick CT images.

TABLE 7. Reconstruction experiment.

Triangular patch	Average surface reconstruction time
1300000±100000	23.64s
600000±50000	10.80s
400000±10000	8.72s

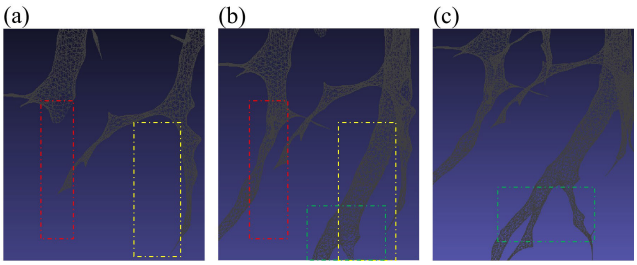

FIGURE 13. The process of generating triangular patches from ordered point sets.

The sparse coding algorithm requires unsupervised learning of the unlabeled images based on the VESSEL12 dataset. The extracted features have certain limitations. Although it can achieve good classification results for the same type of CT, the generalization ability of the model is deficient for other sources and types of data. Visualization of vessel segmentation is shown in Fig. 12, panels (b) and (c), showing the generalization ability of the algorithm even for CT slices with different thicknesses, and complete segmentation of the vessels in the slices.

C. PULMONARY VESSEL RECONSTRUCTION

The experiment was conducted according to the previous description of step C, based on the segmentation results obtained in steps A and B. The experimental variables were the density of triangular patches between adjacent vessel contours and the time required for reconstruction. Each group conducted five experiments. The results are shown in the following table.

The time required for surface reconstruction is related to the number of triangles required by the target.

As shown in Fig. 13, the corresponding colored dotted line box represents the growth process of the reconstructed triangles in the direction of the horizontal section. The correspond-

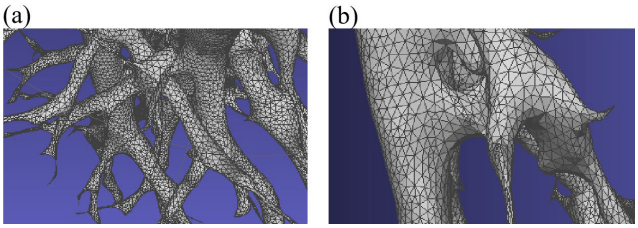

FIGURE 14. Surface triangle patch surrounding.

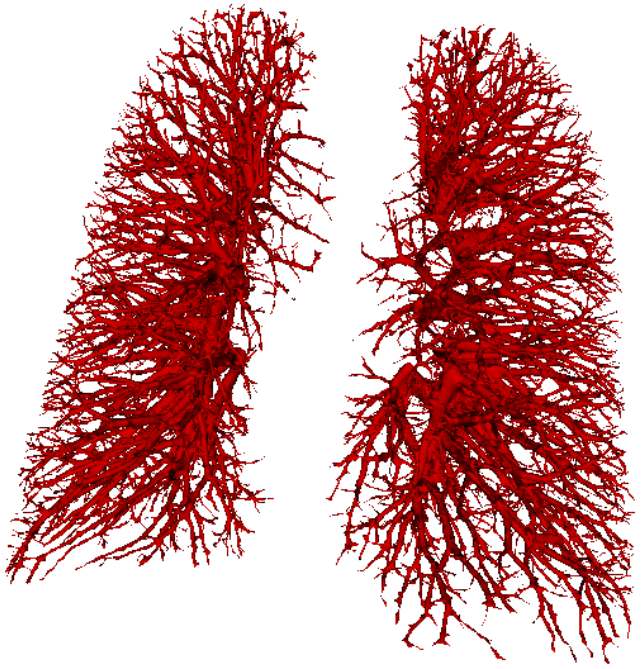

FIGURE 15. Pulmonary vessel tree obtained by 3D reconstruction.

ing triangular patches were generated based on the triangle groups; post-processing operations such as smoothing and texture mapping were performed, as shown in Fig. 14.

After common model post-processing, we obtained the 3D reconstruction result, shown in Fig. 15.

V. CONCLUSION

In this study, an efficient visualization method for pulmonary vessels was demonstrated, in two major parts: vessel segmentation and three-dimensional (3D) reconstruction. The segmentation combined self-supervised and transfer learning. The designed model was pre-trained to effectively extract the features of the pulmonary vessels. The features were transferred to the sparse vessel classification problem. The pulmonary vessel segmentation results were outstanding. The reconstruction, based on the interpolation reconstruction of the segmentation results, saved considerable time in reconstruction of unordered point sets in surface rendering and significantly improved the timeliness of surface reconstruction. For the dataset used in this study, the accuracy of pulmonary vascular contour segmentation reached 98.65% (27,270 test sample points); the classifier evaluation index reached 98.26%, and the average running time of the model was 44 ms. The average time of 3D reconstruction was 10.8 s × 1 1.6 s. Thus, the method proposed in this study has great potential for mainstream treatment of pulmonary diseases, providing fast and accurate guidance for preoperative path planning and intraoperative assistance. Finally, the segmentation and reconstruction methods in this study may be less in thicker CT sequences because generation of positive samples in the self-supervised model and the precision of point-cloud densification in surface rendering depend on the thickness of CT images; this can be further studied in future research.

REFERENCES

[1] C. P. Wild, E. Weiderpass, and B. W. Stewart, *World Cancer Report: Cancer Research For Cancer Prevention*. Lyon, France: International Agency for Research on Cancer, 2020.
[2] J.-M. Naccache, Q. Gibiot, I. Monnet, M. Antoine, M. Wislez, C. Chouaid, and J. Cadranel, "Lung cancer and interstitial lung disease: A literature review," *J. Thoracic Disease*, vol. 10, no. 6, pp. 3829–3844, 2018.
[3] S. Zhang et al., "Cancer incidence and mortality in China," *J. Nat. Cancer Center*, vol. 1, pp. 2–11, 2015.
[4] F. Zhao, Y. Chen, Y. Hou, and X. He, "Segmentation of blood vessels using rule-based and machine-learning-based methods: A review," *Multimedia Syst.*, vol. 25, no. 2, pp. 109–118, Apr. 2019.
[5] Y. He, "Present situation and challenge of convolutional neural network in medical image segmentation," *Comput. Netw.*, vol. 46, no. 17, pp. 2–11, 2020.
[6] M. H. Hesamian, W. Jia, X. He, and P. Kennedy, "Deep learning techniques for medical image segmentation: Achievements and challenges," *J. Digit. Imag.*, vol. 32, no. 4, pp. 582–596, 2019.
[7] P. Zhang, Y. Zhong, Y. Deng, X. Tang, and X. Li, "A survey on deep learning of small sample in biomedical image analysis," 2019, *arXiv:1908.00473*.
[8] H. Kobayashi, K. C. Cheveralls, M. D. Leonetti, and L. A. Royer, "Self-supervised deep learning encodes high-resolution features of protein subcellular localization," *Nature Methods*, vol. 19, no. 8, pp. 995–1003, Aug. 2022.
[9] P. N. Srinivasu and V. E. Balas, "Self-learning network-based segmentation for real-time brain M.R. Images through HARIS," *PeerJ Comput. Sci.*, vol. 7, p. e654, Aug. 2021.
[10] B. M. Mahmmod, S. H. Abdulhussain, M. A. Naser, M. Alsabah, A. Hussain, and D. Al-Jumeily, "3D object recognition using fast overlapped block processing technique," *Sensors*, vol. 22, no. 23, p. 9209, Nov. 2022.
[11] A. Maafiri, O. Elharrouss, S. Rfifi, S. A. Al-Maadeed, and K. Chougdali, "DeepWTPCA-L1: A new deep face recognition model based on WTPCA-L1 norm features," *IEEE Access*, vol. 9, pp. 65091–65100, 2021.
[12] P.-T. Yap, R. Paramesran, and S.-H. Ong, "Image analysis by Krawtchouk moments," *IEEE Trans. Image Process.*, vol. 12, no. 11, pp. 1367–1377, Nov. 2003.
[13] S. H. Abdulhussain, B. M. Mahmmod, T. Baker, and D. Al-Jumeily, "Fast and accurate computation of high-order tchebichef polynomials," *Concurrency Comput., Pract. Exper.*, vol. 34, no. 27, pp. 34–27, Dec. 2022.
[14] B. M. Mahmmod, S. H. Abdulhussain, T. Suk, and A. Hussain, "Fast computation of Hahn polynomials for high order moments," *IEEE Access*, vol. 10, pp. 48719–48732, 2022.
[15] B. Li and X. Zhang, "A pitch estimation algorithm for speech in complex noise environments based on the radon transform," *IEEE Access*, vol. 11, pp. 9876–9889, 2023.
[16] I. Ahmed, A. Khalil, I. Ahmed, and J. Frnda, "Sparse signal representation, sampling, and recovery in compressive sensing frameworks," *IEEE Access*, vol. 10, pp. 85002–85018, 2022.
[17] A. Agarwal and V. Khandelwal, "Multiple manipulation detection in images using frequency domain features in 3D-CNN," *Arabian J. Sci. Eng.*, Mar. 2023.
[18] C.-F.-J. Kuo, J. Barman, C. W. Hsieh, and H.-H. Hsu, "Fast fully automatic detection, classification and 3D reconstruction of pulmonary nodules in CT images by local image feature analysis," *Biomed. Signal Process. Control*, vol. 68, Jul. 2021, Art. no. 102790.

[19] A. Guariento, C. Cattapan, E. Chemello, F. Bertelli, M. Padalino, E. Reffo, G. Di Salvo, R. Motta, and V. L. Vida, "3D reconstruction for preoperative planning of partial anomalous pulmonary venous return," *Kardiologia Polska*, vol. 79, no. 11, pp. 1271–1273, Nov. 2021.

[20] J. Kuriata, P. Kwiatek, P. Kołsut, M. Sterliński, and M. Kuśmierczyk, "Supracardiac partial anomalous pulmonary venous connection recognized by computed tomography in an adult patient," *Kardiol. Polska*, vol. 78, no. 12, pp. 1299–1300, Dec. 2020.

[21] P. Gać, P. Macek, B. Dziadkowiec, B. Kędzierski, and R. Poręba, "Multiple atrial septal defects with concomitant partial anomalous pulmonary venous return on cardiac computed tomography," *Kardiol. Polska*, vol. 78, no. 4, pp. 348–349, Apr. 2020.

[22] D. Mitsouras, P. Liacouras, A. Imanzadeh, A. A. Giannopoulos, T. Cai, K. K. Kumamaru, E. George, N. Wake, E. J. Caterson, B. Pomahac, V. B. Ho, G. T. Grant, and F. J. Rybicki, "Medical 3D printing for the radiologist," *Radiographics*, vol. 35, no. 7, 2015, Art. no. 19651988.

[23] C. Cattapan, F. Bertelli, A. Guariento, M. Andolfatto, P. Veronese, and V. L. Vida, "3D ultrasound-based fetal heart reconstruction: A pilot protocol in prenatal counselling," *Revista Espanola de Cardiologia*, vol. 74, no. 6, pp. 549–551, 2021.

[24] Z. Bian et al., "Overview of anatomical structure segmentation methods in lung CT images," *J. Image Graph.*, vol. 23, no. 10, pp. 1450–1471, 2018.

[25] Y. Sato, S. Nakajima, H. Atsumi, T. Koller, G. Gerig, S. Yoshida, and R. Kikinis, "3D multi-scale line filter for segmentation and visualization of curvilinear structures in medical images," in *Proc. Int. Conf. Comput. Vis., Virtual Reality, Robot. Med.* Berlin, Germany: Springer, 1997, pp. 213–222.

[26] A. F. Frangi, W. J. Niessen, K. L. Vincken, and M. A. Viergever, "Multiscale vessel enhancement filtering," in *Medical Image Computing and Computer-Assisted Intervention—MICCAI*. Berlin, Germany: Springer, 1998.

[27] R. D. Rudyanto et al., "Comparing algorithms for automated vessel segmentation in computed tomography scans of the lung: The VESSEL12 study," *Med. Image Anal.*, vol. 18, no. 7, pp. 1217–1232, Oct. 2014.

[28] B. Lassen, M. Schmidt, S. Kerkstra, B. van Ginneken, J.-M. Kuhnigk, and E. van Rikxoort, "Automatic segmentation of the pulmonary lobes from chest CT scans based on fissures, vessels, and bronchi," *IEEE Trans. Med. Imag.*, vol. 32, no. 2, pp. 210–222, Feb. 2013.

[29] R. Adams and L. Bischof, "Seeded region growing," *IEEE Trans. Pattern Anal. Mach. Intell.*, vol. 16, no. 6, pp. 641–647, Jun. 1994.

[30] W. Tan, Y. Yuan, A. Chen, L. Mao, Y. Ke, and X. Lv, "An approach for pulmonary vascular extraction from chest CT images," *J. Healthcare Eng.*, vol. 2019, pp. 1–11, Jan. 2019.

[31] J. N. Kaftan, A. P. Kiraly, A. Bakai, M. Das, C. L. Novak, and T. Aach, "Fuzzy pulmonary vessel segmentation in contrast enhanced CT data," *Proc. SPIE*, vol. 6914, Mar. 2008, Art. no. 69141Q.

[32] M. Orkisz, M. H. Hoyos, V. P. Romanello, C. P. Romanello, J. C. Prieto, and C. Revol-Müller, "Segmentation of the pulmonary vascular trees in 3D CT images using variational region-growing," *IRBM*, vol. 35, no. 1, pp. 11–19, Feb. 2014.

[33] T. Lv, G. Yang, Y. Zhang, J. Yang, Y. Chen, H. Shu, and L. Luo, "Vessel segmentation using centerline constrained level set method," *Multimedia Tools Appl.*, vol. 78, no. 12, pp. 17051–17075, Jun. 2019.

[34] S. Moccia, E. De Momi, S. El Hadji, and L. S. Mattos, "Blood vessel segmentation algorithms—Review of methods, datasets and evaluation metrics," *Comput. Methods Programs Biomed.*, vol. 158, pp. 71–91, May 2018.

[35] Q. Pan, "Research on segmentation algorithm of non-uniform gray medical image based on multi-scale level set," China Univ. Sci. Technol., Taipei, Taiwan, Tech. Rep., 2019.

[36] B. Zhao, Z. Cao, and S. Wang, "Lung vessel segmentation based on random forests," *Electron. Lett.*, vol. 53, no. 4, pp. 220–222, Feb. 2017.

[37] R. Ochs, J. Goldin, F. Abtin, H. Kim, K. Brown, P. Batra, D. Roback, M. Mcnittgray, and M. Brown, "Automated classification of lung bronchovascular anatomy in CT using AdaBoost," *Med. Image Anal.*, vol. 11, no. 3, pp. 315–324, Jun. 2007.

[38] X. Gu, J. Wang, J. Zhao, and Q. Li, "Segmentation and suppression of pulmonary vessels in low-dose chest CT scans," *Med. Phys.*, vol. 46, no. 8, pp. 3603–3614, Aug. 2019.

[39] Y. Xu, Z. Mao, C. Liu, and B. Wang, "Pulmonary vessel segmentation via stage-wise convolutional networks with orientation-based region growing optimization," *IEEE Access*, vol. 6, pp. 71296–71305, 2018.

[40] A. Wu, Z. Xu, M. Gao, M. Buty, and D. J. Mollura, "Deep vessel tracking: A generalized probabilistic approach via deep learning," in *Proc. IEEE 13th Int. Symp. Biomed. Imag. (ISBI)*, Apr. 2016, pp. 1363–1367.

[41] M. Kazhdan, M. Bolitho, and H. Hoppe, "Poisson surface reconstruction," in *Proc. Eurograph. Symp. Geometry Process.*, vol. 6, 2006, pp. 61–70.

[42] H. Hoppe, T. DeRose, T. Duchamp, J. McDonald, and W. Stuetzle, "Surface reconstruction from unorganized points," in *Proc. 19th Annu. Conf. Comput. Graph. Interact. Techn. (SIGGRAPH)*, 1992, pp. 71–78.

[43] C. Shen, J. F. O'Brien, and J. R. Shewchuk, "Interpolating and approximating implicit surfaces from polygon soup," in *Proc. ACM SIGGRAPH Papers*, Aug. 2004.

[44] F. Bernardini, J. Mittleman, H. Rushmeier, C. Silva, and G. Taubin, "The ball-pivoting algorithm for surface reconstruction," *IEEE Trans. Vis. Comput. Graphics*, vol. 5, no. 4, pp. 349–359, Oct. 1999.

[45] C.-C. Kuo and H.-T. Yau, "A delaunay-based region-growing approach to surface reconstruction from unorganized points," *Comput.-Aided Des.*, vol. 37, no. 8, pp. 825–835, Jul. 2005.

[46] E. Keppel, "Approximating complex surfaces by triangulation of contour lines," *IBM J. Res. Develop.*, vol. 19, no. 1, pp. 2–11, Jan. 1975.

[47] H. Fuchs, Z. M. Kedem, and S. P. Uselton, "Optimal surface reconstruction from planar contours," *Commun. ACM*, vol. 20, no. 10, pp. 693–702, Oct. 1977.

[48] Z. Cui, C. Ding, C. Li, X. Song, J. Chen, T. Chen, C. Xu, and J. Zhao, "Preoperative evaluation of the segmental artery by three-dimensional image reconstruction vs. thin-section multi-detector computed tomography," *J. Thoracic Disease*, vol. 12, no. 8, pp. 4196–4204, Aug. 2020.

[49] N. Ikeda, A. Yoshimura, M. Hagiwara, S. Akata, and H. Saji, "Three dimensional computed tomography lung modeling is useful in simulation and navigation of lung cancer surgery," *Ann. Thoracic Cardiovascular Surg.*, vol. 19, no. 1, p. 15, 2013.

[50] J. Le Moal et al., "Cancer incidence and mortality in China," in *Three-Dimensional Computed Tomography Reconstruction for Operative Planning in Robotic Segmentectomy: A Pilot Study*, 2018, pp. 196–201.

[51] K. Guggenberger, A. J. Krafft, U. Ludwig, E. Raithel, C. Forman, S. Meckel, J. Hennig, T. A. Bley, and P. Vogel, "Intracranial vessel wall imaging framework—Data acquisition, processing, and visualization," *Magn. Reson. Imag.*, vol. 83, pp. 114–124, Nov. 2021.

[52] P. Vogel et al., "Robust centerline prediction for accurate vessel wall visualization of intracranial vessels in multi-contrast 3D MRI data," *Med. Phys.*, 2022.

[53] V. I. Kigka, G. Rigas, A. Sakellarios, P. Siogkas, I. O. Andrikos, T. P. Exarchos, D. Loggitsi, C. D. Anagnostopoulos, L. K. Michalis, D. Neglia, G. Pelosi, O. Parodi, and D. I. Fotiadis, "3D reconstruction of coronary arteries and atherosclerotic plaques based on computed tomography angiography images," *Biomed. Signal Process. Control*, vol. 40, pp. 286–294, Feb. 2018.

[54] C. Fu, R. Guo, D. Yang, H. Wang, and X. Zhang, "Automatic 3D reconstruction of carotid vessels based on region growing method," in *Proc. 11th Int. Conf. Inf. Commun. Technol. (ICTech)*, Feb. 2022, pp. 446–450.

[55] F. Fu, J. Wei, M. Zhang, F. Yu, Y. Xiao, D. Rong, Y. Shan, Y. Li, C. Zhao, F. Liao, Z. Yang, Y. Li, Y. Chen, X. Wang, and J. Lu, "Rapid vessel segmentation and reconstruction of head and neck angiograms using 3D convolutional neural network," *Nature Commun.*, vol. 11, no. 1, p. 4829, Sep. 2020.

[56] X. Li, X. Wang, Y. Dai, and P. Zhang, "Supervised recursive segmentation of volumetric CT images for 3D reconstruction of lung and vessel tree," *Comput. Methods Programs Biomed.*, vol. 122, no. 3, pp. 316–329, Dec. 2015.

[57] Ö. Çiçek, A. Abdulkadir, S. S. Lienkamp, T. Brox, and O. Ronneberger, "3D U-Net: Learning dense volumetric segmentation from sparse annotation," in *Proc. Int. Conf. Med. Image Comput. Comput.-Assist. Intervent.* Cham, Switzerland: Springer, 2016, pp. 424–432.

[58] A. Vulli, P. N. Srinivasu, M. S. K. Sashank, J. Shafi, J. Choi, and M. F. Ijaz, "Fine-tuned DenseNet-169 for breast cancer metastasis prediction using FastAI and 1-cycle policy," *Sensors*, vol. 22, no. 8, p. 2988, Apr. 2022.

[59] T. Konopczynski, T. Kroger, L. Zheng, C. S. Garbe, and J. Hesser, "Automated multiscale 3D feature learning for vessels segmentation in thorax CT images," in *Proc. IEEE Nucl. Sci. Symp., Med. Imag. Conf. Room-Temp. Semiconductor Detect. Workshop (NSS/MIC/RTSD)*, Oct. 2016, pp. 1–3.

QIANGHAO HUANG was born in 1997. He received the M.S. degree in control engineering from Zhejiang University, Hangzhou, China. He is currently a Research Assistant with the College of Control Science and Engineering, Zhejiang University. He has authored or coauthored three books to robotics and applied for six national invention patents. His research interests include medical robot, image process, and manifold learning. He is a Liaison Member of the International Alliance of Robotics Associations. He received the national scholarship in China, in 2018.

LIN ZHANG was born in 1996. She received the M.Eng. degree from the College of Control Science and Engineering, Zhejiang University, Hangzhou, China, in 2021. Her research interests include medical image processing and surgical robotics.

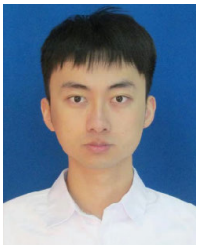

LILU LIU was born in 1997. He received the B.Eng. degree from the School of Electrical Engineering and Automation, Harbin Institute of Technology, Harbin, China, in 2019. He is currently pursuing the Ph.D. degree with the College of Control Science and Engineering, Zhejiang University, Hangzhou, China. His research interests include medical image analysis, object pose estimation, and surgical robotics.

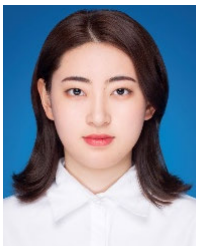

YUQI CAO was born in 1994. She received the Ph.D. degree from the College of Control Science and Engineering, Zhejiang University, Hangzhou, China, in 2022. In 2019, she was a Visiting Student with the Xi-Cheng Zhang's Group for one year with the Institute of Optics, University of Rochester, Rochester, NY, USA. She is currently an Associate Research Fellow with the College of Control Science and Engineering, Zhejiang University. She has authored or coauthored 13 journal articles and eight conference papers. Her research interests include medical image processing, advanced transducer and measurement, and THz-based human cancer detection.

HONGHAI MA was born in 1987. He received the B.S. degree in clinical medicine and the master's and Ph.D. degrees in surgery, in 2010, 2014, and 2018, respectively. He is currently with the Department of Thoracic Surgery, The First Affiliated Hospital, Zhejiang University School of Medicine. His research interests include basic and clinical research of lung cancer and inventions of surgical instruments.

LUMING WANG was born in 1982. He received the B.S., M.S., and Ph.D. degrees from the Medical College of Zhejiang University, in 2005, 2007, and 2017, respectively. He is currently the Deputy Chief Physician of the General Thoracic Surgery Department, The First Affiliated Hospital, Zhejiang University School of Medicine. He has authored or coauthored more than 50 papers and participated in the compilation of four books. His research interest includes the diagnosis and treatment of various diseases in thoracic surgery.

CHUNLIN ZHOU was born in 1980. He received the B.Eng. and M.Eng. degrees in mechatronics engineering from Shanghai Jiao Tong University, China, in 2003 and 2006, respectively, and the Ph.D. degree in mechatronics from Nanyang Technological University, Singapore, in 2012. He is currently an Associate Professor with Zhejiang University, China. His research interests include mechatronics of robotic systems, bionic robots, and surgical robots.